Three-dimensional refractive index tomograms and deformability of individual human red blood cells from cord blood of newborn infants and maternal blood

HyunJoo Park
Taegyu Ahn
Kyoohyun Kim
Sangyun Lee
Song-yi Kook
Dongheon Lee
In Bum Suh
Sunghun Na
YongKeun Park

Three-dimensional refractive index tomograms and deformability of individual human red blood cells from cord blood of newborn infants and maternal blood

HyunJoo Park,[a,†] **Taegyu Ahn,**[b,†] **Kyoohyun Kim,**[a] **Sangyun Lee,**[a] **Song-yi Kook,**[b] **Dongheon Lee,**[b]
In Bum Suh,[c] **Sunghun Na,**[b,*] **and YongKeun Park**[a,*]
[a]Department of Physics, Korea Advanced Institute of Science and Technology, Daejeon 305-701, Republic of Korea
[b]Kangwon National University, Department of Obstetrics and Gynecology, Kangwon National University Hospital, School of Medicine, Chuncheon 200-701, Republic of Korea
[c]Kangwon National University, Department of Laboratory Medicine, Kangwon National University Hospital, School of Medicine, Chuncheon 200-701, Republic of Korea

Abstract. Red blood cells (RBCs) from the cord blood of newborn infants have distinctive functions in fetal and infant development. To systematically investigate the biophysical characteristics of individual cord RBCs in newborn infants, a comparative study was performed on RBCs from the cord blood of newborn infants and from adult mothers or nonpregnant women using optical holographic microtomography. Optical measurements of the distributions of the three-dimensional refractive indices and the dynamic membrane fluctuations of individual RBCs were used to investigate the morphological, biochemical, and mechanical properties of cord, maternal, and adult RBCs at the individual cell level. The volume and surface area of the cord RBCs were significantly larger than those of the RBCs from nonpregnant women, and the cord RBCs had more flattened shapes than that of the RBCs in adults. In addition, the hemoglobin (Hb) content in the cord RBCs from newborns was significantly higher. The Hb concentration in the cord RBCs was higher than that in the nonpregnant women or maternal RBCs, but they were within the physiological range of adults. Interestingly, the amplitudes of the dynamic membrane fluctuations in cord RBCs were comparable to those in nonpregnant women and maternal RBCs, suggesting that the deformability of cord RBCs is similar to that of healthy RBCs in adults. © *2015 Society of Photo-Optical Instrumentation Engineers (SPIE)* [DOI: 10.1117/1.JBO.20.11.111208]

1 Introduction

After birth, a newborn infant's circulatory system starts after disconnection of the umbilical cord, which was used for oxygen and nutrient transport from the placenta of the mother. The cord blood left in the umbilical cord of newborn infants has the characteristics of fetal blood at full term, and characterizing individual cord red blood cells (RBCs) from newborn infants is crucial in understanding maternal-fetal circulation and fetus development and in opening up new possibilities for diagnosing the diseases of newborn infants.[1]

Previous studies have revealed that cord RBCs from newborn infants are significantly different from those in adult blood. For example, macrocytic RBCs, enlarged RBCs with a mean corpuscular volume (MCV) > 110 fL, are predominant in neonatal blood,[2] although capillary sizes in newborn infants are similar to those in adults.[3] The cytoplasm of cord RBCs is mainly composed of fetal hemoglobin (HbF) rather than adult hemoglobin (HbA); HbF exhibits a higher oxygen binding affinity than that of HbA.[4–6] The life span of cord RBCs (60 to 80 days) is significantly shorter than normal RBCs (120 days).[7] The

aforementioned characteristics of cord RBCs dramatically change within the first 12 weeks after birth[8] by producing RBCs with HbA instead of HbF.

Biochemical characterization of cord RBCs and HbF has been extensively studied, but our understanding of cord RBCs in newborn infants remains incomplete. In particular, the morphological and mechanical properties of cord RBCs in newborn infants, which are closely related to the deformability of cord RBCs and cord-blood circulation, have not been fully addressed largely because of the limitations in measurement techniques. For example, different techniques have led to different interpretations of the deformability of cord RBCs. Previous work using light scattering or hemolysis techniques have reported that cord RBCs are more deformable than adult RBCs,[9,10] whereas electron spin resonance and filtration studies have concluded that there are no significant differences in cell deformability between cord RBCs and adult RBCs.[11–13]

Quantitative phase imaging (QPI), however, circumvents the limitations of previous measurement techniques and offers unique advantages to precisely measure the morphological and mechanical properties of cord RBCs. QPI techniques enable quantitative, noninvasive measurements of optical phase-delay maps induced by transparent samples (e.g., biological cells and

---

*Address all correspondences to: YongKeun Park, E-mail: yk.park@kaist.ac.kr; Sunghun Na, E-mail: lahun@kangwon.ac.kr

†These authors contributed equally to this work.

tissues).[14–17] These QPI techniques have been utilized to study the pathophysiology of RBCs and provide unique advantages.[18–21] With three-dimensional (3-D) QPI techniques, measuring the 3-D refractive index (RI) distributions of individual RBCs can be done, which provide morphological (cell volume, surface area, and sphericity) and biochemical (Hb content and concentration) information about individual RBCs. This is because the RBC cytoplasm is mainly an Hb solution, and the RI of an Hb solution is linearly proportional to its concentration.[22] In addition, the dynamic fluctuation in RBC membranes can be precisely measured using QPI techniques, which provides information about the biomechanical properties of the membrane cortex and the cytoplasm.[23–27] Recently, QPI techniques have been used to study the pathophysiology of RBCs, including osmotic changes,[28] malaria infection,[25,29,30] sickle cell disease,[21,27] and ATP-dependent morphological remodeling.[23,31]

Here, we report the optical measurements for the morphological, biochemical, and mechanical properties of cord RBCs in newborn infants. With optical holographic microtomography, 3-D RI tomograms and dynamic membrane fluctuations of individual RBCs were noninvasively and quantitatively measured at the individual cell level. From the measured RI tomograms, the morphological (cell volume, surface area, and sphericity) and biochemical (Hb content and concentration) parameters were retrieved. For a comparative study, optical measurements were done for RBCs collected from the blood of nonpregnant women, from the cord blood of full-term newborn infants (within 5 min after delivery), and from maternal blood. The 3-D RI tomographic maps and the obtained biophysical parameters clearly show the distinctive morphologies of the cord RBCs, including large volumes and more flattened discocyte shapes, while the maternal RBCs showed elliptical shapes from the loss of the dimple. In addition, the measured dynamic membrane fluctuations showed that the cord RBCs have cellular deformability comparable to the RBCs from maternal and nonpregnant women.

2 Materials and Methods

2.1 Ethics Statement

Human blood studies were conducted according to the principles of the Declaration of Helsinki and were approved by the responsible ethics committee of Kangwon National University Hospital (IRB project number: 2012-0128, Chuncheon, Republic of Korea) before the start of the study. Human blood was collected from both nonpregnant women and healthy term pregnant women who were 20 years of age or older and had signed a written informed consent form explaining that the blood would be used for academic research purposes. The blood of nonpregnant women was obtained during regular medical checkups done at the Health Promotion Center of a hospital after approval in accordance with the procedures of IRB for remaining blood. Maternal blood and cord blood from newborn infants were also collected after receiving both written consent directly from both the mother on behalf of herself and her baby and verbal consent from the caretakers or guardians of the minors/children enrolled in the study. This consent form was also approved by the IRB committee. The collection method for cord blood had minimum risk to the babies and their mothers because the cord blood was collected from the umbilical cord in the placenta after the umbilical cord of the baby was detached from the placenta.

2.2 Maternal and Cord Blood Collection

Blood samples were collected for healthy term pregnant women at Kangwon National University Hospital. Cord blood collections were performed by an obstetrician who was attending the delivery. The umbilical vein of a newborn infant was punctured within 5 min after delivery, and 2 mL of cord blood was collected in anticoagulant agent K2 EDTA (ethylenediaminetetraacetic acid) Vacutainer (BD, New Jersey). The maternal blood was sampled on the day of the birth, and the blood from nonpregnant women was obtained from the remaining blood after an examination at a health promotion center at Kangwon National University Hospital. All subjects were healthy without any complications. The total population consisted of three nonpregnant women as the control and five pairs of newborn infants and their mothers. For the optical measurements, the blood samples were further diluted 300 times in *Dulbecco's* phosphate buffer saline buffer (Gibco®, New York).

2.3 Common-Path Diffraction Optical Tomography

The optical setup for common-path diffraction optical tomography (cDOT) is described in more detail in a previous study.[32,33] cDOT is an optical system for holographic microtomography, which has the capability of measuring the 3-D RI distribution of a sample with high precision. cDOT measures multiple two-dimensional (2-D) optical fields of a sample from different illumination angles, from which the 3-D RI tomogram of the sample $n(x, y, z)$ is reconstructed using a DOT algorithm. Recently, cDOT has been utilized for the characterization of red blood cells,[34] white blood cells,[35,36] phytoplankton,[37] and hairs.[38]

Briefly, a diode-pumped solid-state laser ($\lambda = 532$ nm, 50 mW, Cobalt, Solna, Sweden) was used as an illumination source. By rotating a two-axis galvanometer mirror (GVS012/M, Thorlabs, USA), the angle of the incident beam was varied. For 3-D RI tomography, the optical fields at various incident illumination angles were measured with common-path laser-interferometric microscopy.

The sample, diluted blood sandwiched between two cover glasses 25×50 mm (C025501, MATSUNAMI GLASS Ind., Ltd., Japan) was placed between the condenser lens [UPLSAPO 60×, numerical aperture (N.A.) = 0.9, Olympus, Japan] and objective lens (UPLSAPO 60×, N.A. = 1.42, Olympus, Japan). The second galvanometer mirror reflected the beam from the sample to have the same optical path regardless of the incident illumination angle. After the second galvanometer mirror, a diffraction grating (92 grooves mm^{-1}, #46-072, Edmund Optics Inc., New Jersey) spatially split the scattering beams and then the spatially filtered zeroth-order beam as the reference interfered with the first-order beam as the sample beam. Then, interferograms were recorded on a high-speed sCMOS camera (Neo sCMOS, ANDOR Inc., Northern Ireland) while the incident beam was scanning spirally with 300 different angles. The total magnification was 240 by an additional 4-f system. From the measured optical fields, the 3-D RI distribution of the sample was reconstructed using an optical diffraction tomography algorithm described elsewhere.[39,40]

2.4 Analysis of the Red Cell Parameters

The six red cell parameters consisted of morphological (cell volume, surface area, and sphericity), chemical (Hb content and Hb concentration), and mechanical (membrane fluctuations)

properties.[36] To measure the morphological parameters, we used the reconstructed 3-D RI maps from the diffraction optical tomography algorithm using multiple measured optical phase maps corresponding to various illumination angles on the sample. The whole volume of an RBC was calculated by integrating all voxels inside individual RBCs. The space corresponding to the cytoplasm of an RBC was selected by RI with a higher value than the threshold. The threshold was defined as 50% of the RI difference between the maximum RI of the cell $n$cell_max and the surrounding medium nm to determine the cell boundary, i.e., $n$thresh $= n$m $+ 0.5$ ($n$cell_max $-n$m). Then, the total number of voxels was multiplied by the magnification of the optical system to translate in a length scale. Next, for the surface area measurements, the isosurfaces of individual RBCs were reconstructed from the volume data of the 3-D RI maps with MATLAB®. The surface area of the isosurfaces was measured with the sum of the areas of all the patch faces, which were broken down into small triangular pieces. In addition, the sphericity SI, a dimensionless quantity ranging from 0 to 1, was obtained as follows: $\text{SI} = \pi^{1/3}(6V)^{2/3}/A$, where V is the volume and A is the surface area.[34,41]

To measure the Hb content, the measured 2-D phase at the normal angle was used.[22,42] The Hb content of an RBC was obtained from integrating the 2-D optical phase over the entire cell area with the RI increment of the proteins.

$$\text{Hb content} = \frac{\lambda}{2\pi\alpha}\sum \Delta\phi(x, y), \qquad (1)$$

where λ is the wavelength of the laser light (532 nm); α is the RI increment (0.2 mL/g),[43,44] and $\Delta\phi(x, y)$ is the 2-D optical phase. In addition, the Hb concentration in RBC was obtained from the Hb content divided by the cellular volume.

The dynamic membrane fluctuations in RBCs can be quantitatively and precisely measured using cDOT. Consecutive dynamic full-field optical phase images of RBC $\Delta\phi(x, y, t)$

can be measured with normal laser illumination, from which dynamic height maps of the RBC can be calculated as $h(x, y, t) = [\lambda/(2\pi \cdot \Delta n)]\Delta\phi(x, y, t)$, where λ is the wavelength of the illumination laser, and $\Delta n = \langle n(x, y, z)\rangle$-$n$m is the difference between the mean RI of the RBC cytoplasm $\langle n(x, y, z)\rangle$ and the surrounding buffer medium nm.

To measure the mechanical parameter, we calculated the dynamic membrane fluctuation from the successively measured instantaneous height map $h(x, y; t)$, given as

$$h(x, y; t) = \frac{\lambda}{2\pi\Delta n} \cdot \Delta\phi(x, y; t). \qquad (2)$$

The values for the membrane fluctuation were calculated by averaging the root mean square of the height displacement over the cell area, given as

$$\Delta h_{\text{rms}}(x, y) = \langle[h(x, y; t) - h_m(x, y)]^2\rangle^{1/2}, \qquad (3)$$

where h_m is the time-averaged height at the cell surface.

3 Results

3.1 Three-Dimensional Refractive Index Tomograms of Individual Cord and Maternal RBCs

To investigate the 3-D morphological details of individual RBCs, we used cDOT (see Sec. 2). Using cDOT, the 3-D RI distributions of individual RBCs were measured. Samples were collected from three nonpregnant women (121 RBCs), and from five full-term newborn infants (215 RBCs) and their mothers (181 RBCs) after delivery. Then, the RBCs were subjected to quantitative, noninvasive measurements.

The 3-D RI maps of typical RBCs from each group are shown in Figs. 1(a)–1(f). The cord RBCs from newborn infants
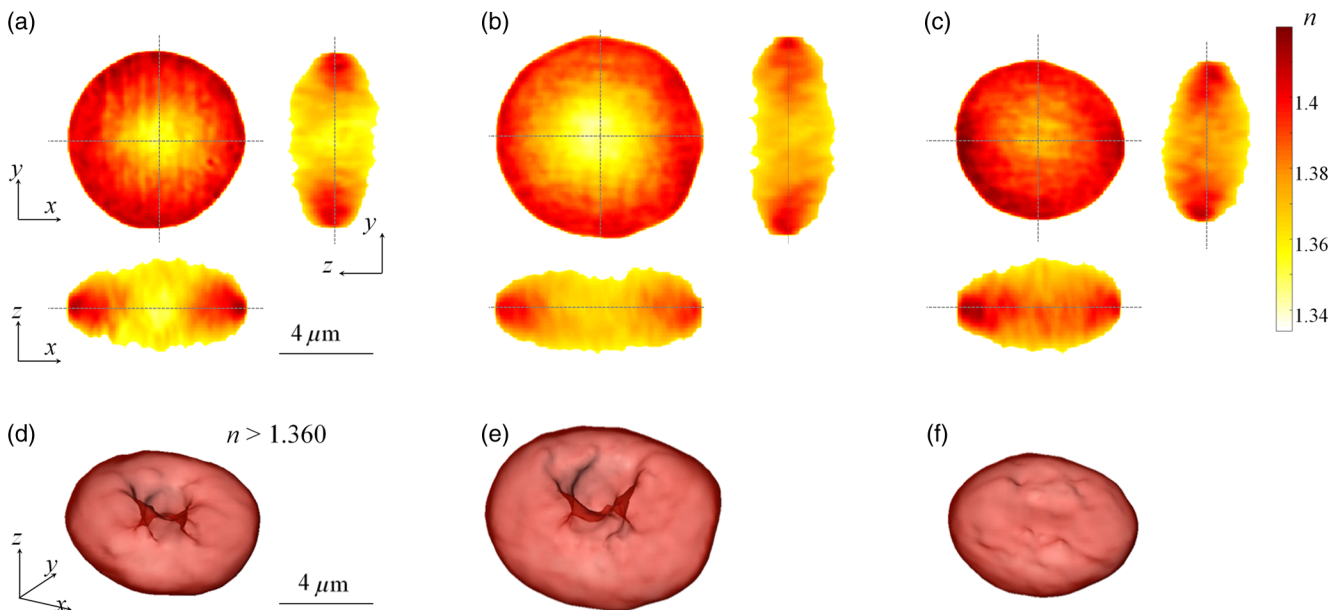
Fig. 1 (a) to (c) Reconstructed three-dimensional (3-D) refractive index (RI) tomograms of (a) the RBCs from a healthy nonpregnant woman, (b) a RBC from the cord blood, and (c) RBC from a mother, respectively. The cross-sectional slices of the RI tomograms are shown in the $x-y$ (top left panel), $y-z$ (right panel), and $x-z$ (bottom panel) planes. (d) to (f) 3-D rendered isosurface images of the RBCs in (a) to (c).

are enlarged compared to the RBCs from nonpregnant women. The RBCs from the corresponding mothers, the maternal RBCs, are smaller than the cord RBCs, and even smaller than the RBCs from nonpregnant women. Interestingly, the inner dimple area was absent in the maternal RBCs while the cord RBCs were biconcave discocytes. The characteristic doughnut shapes and loss of biconcave areas can easily be seen in the rendered iso-surfaces of the 3-D RI maps [Figs. 1(d)–1(f)].

3.2 Quantitative Morphological Parameters of Individual Cord and Maternal RBCs

For the quantitative analysis, we calculated the morphological parameters from the measured 3-D RI tomograms of the cord and maternal RBCs. These morphological parameters consisted of cellular volume, surface area, and sphericity (see Sec. 2). The cord RBCs of newborn infants had cells that were significantly larger than the RBCs from the nonpregnant women, in terms of both the volume and surface area [Figs. 2(a) and 2(b)]. For the cord RBCs, the mean values for the cell volume and surface area were 99.5 ± 16.8 fL and 181.8 ± 21.9 μm^2, whereas those for the RBCs from the mothers and nonpregnant women were 89.6 ± 8.0 fL and 139.2 ± 17.4 μm^2, and 87.2 ± 13.0 fL and 148.9 ± 16.5 μm^2, respectively. The volumes of the nonpregnant women RBCs measured with cDOT were consistent with the physiological range and the MCV, which were independently measured with automated blood-cell counters based on the complete blood count (CBC). These are indicated by the gray lines in Fig. 2(a). The MCV with the red cell distribution width measured by the CBC were 87.3 ± 15.3, 99.2 ± 14.4, and 89.6 ± 12.2 fL for nonpregnant adult RBCs, cord RBCs, and maternal RBCs, respectively. Note that the surface area cannot be obtained from the CBC measurements. Previously, surface areas for healthy RBCs and cord RBCs have been measured using a micropipette aspiration technique,[45] to which our results are qualitatively consistent. The volume and surface area of the maternal RBCs were comparable to those of the nonpregnant women RBCs [Fig. 2(b)]. The increased volume in the cord RBCs is consistent with previous CBC measurements.[2]

To analyze the degree of biconcave shape in the cord and maternal RBCs quantitatively, we calculated the sphericity from the measured cell volume and surface area. The sphericity is a dimensionless measure of how spherical an object is. The sphericity of a perfect sphere is 1 and that of a flat surface is 0. The mean sphericity value of the RBCs from the nonpregnant women, exhibiting a characteristic biconcave shape, was 0.64 ± 0.06. The sphericity of the cord RBCs and maternal RBCs were 0.57 ± 0.07 and 0.70 ± 0.09, respectively. This result indicates that compared to the healthy RBCs from nonpregnant women, the enlarged cord RBCs had more flattened shapes, and the maternal RBCs were more spherical.

### 3.3 Cellular Hemoglobin Content and Concentration in Individual Cord and Maternal RBCs

To quantify the biochemical characteristics of the RBC cytoplasm, the Hb content and concentration in the cord and maternal RBCs were quantified from the measured 3-D RI maps. The Hb content of individual RBCs was retrieved from the measured 2-D optical field of the cells with cDOT. Then, the Hb concentration of individual RBCs was calculated from the Hb content and cell volume of individual RBCs (see Sec. 2).

The mean values of Hb content were 29.5 ± 4.7, 35.9 ± 6.9, and 30.3 ± 5.2 pg for nonpregnant adult RBCs, cord RBCs, and maternal RBCs, respectively [Fig. 3(a)]. The Hb content in the cord RBCs was 22% greater than that of the RBCs from the nonpregnant women, while the Hb content of the maternal RBCs was comparable to that of the RBCs from the nonpregnant women. This result, obtained with cDOT, is also consistent with the CBC measurements: mean corpuscular hemoglobin values were 29.6 ± 1.2, 34.7 ± 0.6, and 30.7 ± 3.9 pg for the nonpregnant adult RBCs, cord RBCs, and maternal RBCs, respectively [gray dotted lines in Fig. 3(a)].

The mean values for the Hb concentrations were 33.8 ± 2.6, 36.3 ± 4.7, and 34.2 ± 3.3 g/dL for the nonpregnant adult RBCs, cord RBCs, and maternal RBCs, respectively [Fig. 3(b)]. The mean value for the Hb concentration of the cord RBCs was measurably greater than that of RBCs from nonpregnant women, and of maternal RBCs.
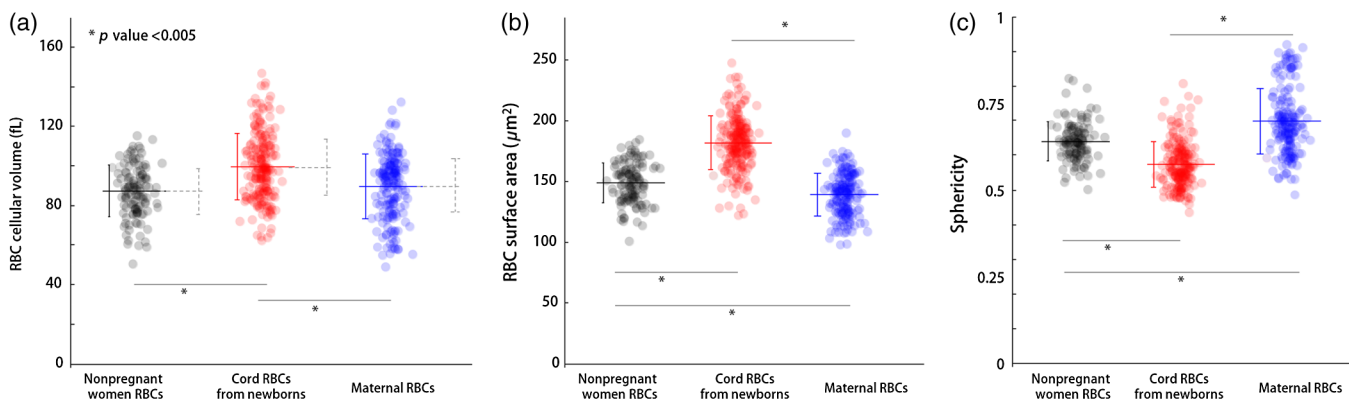
Fig. 2 Red cell indices for nonpregnant women RBCs ($N = 121$, black circles), cord RBCs from full-term newborn infants ($N = 215$, red circles), and their maternal RBCs ($N = 181$, blue circles): (a) cellular volume of the RBCs, (b) surface area of the RBCs, and (c) sphericity index. Each symbol represents an individual RBC measurement; the horizontal solid line is the mean value and the vertical lines are STD error bars. Gray dot lines in (a) correspond to the averaged mean corpuscular volume from the relevant complete blood count (CBC) blood test, with vertical lines for the red cell distribution width. The symbol * indicates a p value <0.005.
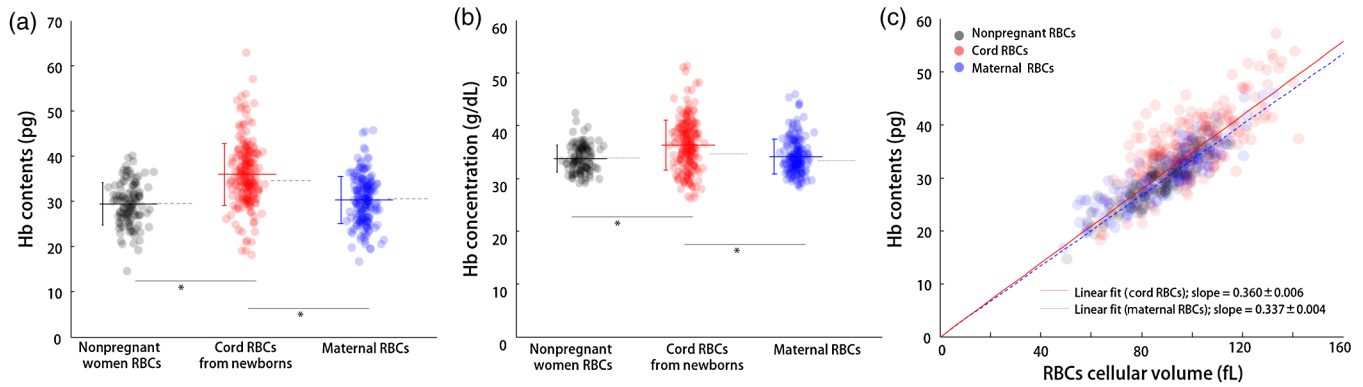
Fig. 3 (a) RBC Hb contents and (b) Hb concentration of nonpregnant women RBCs ($N = 121$, black circles), fetal cord RBCs ($N = 215$, red circles), and maternal RBCs ($N = 181$, blue circles). Each symbol represents an individual RBC measurement; the horizontal line is the mean value and vertical lines indicate STD error bars. Horizontal gray dot lines in (a) and (b) correspond to the averaged mean corpuscular hemoglobin and mean corpuscular Hb concentration from the CBC blood test. (c) Correlation map of RBC cellular volume and RBC Hb contents with fitted linear slopes for the cord RBCs (red solid line) and maternal RBCs (blue dashed line). The symbol * indicates a p value <0.005.

As shown in Fig. 3(c), the correlations between Hb content and cellular volume were positive in all three RBC groups. The linear slope in the correlation map shows the Hb concentration of each RBC group, and the values of the slope were 0.334 ± 0.005, 0.360 ± 0.006, and 0.337 ± 0.004 pg/fL for the RBCs from the nonpregnant women, cord RBCs, and maternal RBCs, respectively. These results are also in good agreement with the CBC measurements: mean corpuscular Hb concentration was found to be 33.9, 34.6, and 33.34 g/dL for the RBCs from the nonpregnant women, cord RBCs, and maternal RBCs, respectively [gray dotted lines in Fig. 3(b)]. Although the Hb concentrations in the cord RBCs were slightly greater, all the mean values of the Hb concentration were within the reference range of a healthy adult (33 to 36 g/dL).

3.4 Cellular Elasticity of Individual Cord and Maternal RBCs

To investigate the mechanical properties or deformability of individual cord and maternal RBCs, the dynamic membrane fluctuations of the RBCs were measured. Due to the soft and elastic properties of the membrane cortex structures, RBCs exhibit dynamic membrane fluctuations driven by thermal or metabolic energy.[23,31,46–49] The dynamic membrane fluctuations manifest as the deformability of RBC membranes, which is strongly correlated with the structures of the lipid membrane and spectrin network, and with alternations caused by various pathophysiological conditions.[19,21,39]

The dynamic membrane fluctuations in the RBCs were quantitatively and precisely measured with cDOT. Consecutive dynamic full-field optical phase images of individual RBCs were measured with normal laser illumination, from which the mean and dynamic height maps of the RBCs were calculated (see Sec. 2). The representative mean and dynamic height maps of individual RBCs in each group are presented in Figs. 4(a)–4(c). Consistent with the results of the 3-D rendered isosurfaces [Figs. 1(d)–1(f)], the mean cell shape results show that the maternal RBCs had spherical shapes without center-dimpled regions, whereas the cord RBCs as well as the nonpregnant women RBCs had the characteristic donut shape.
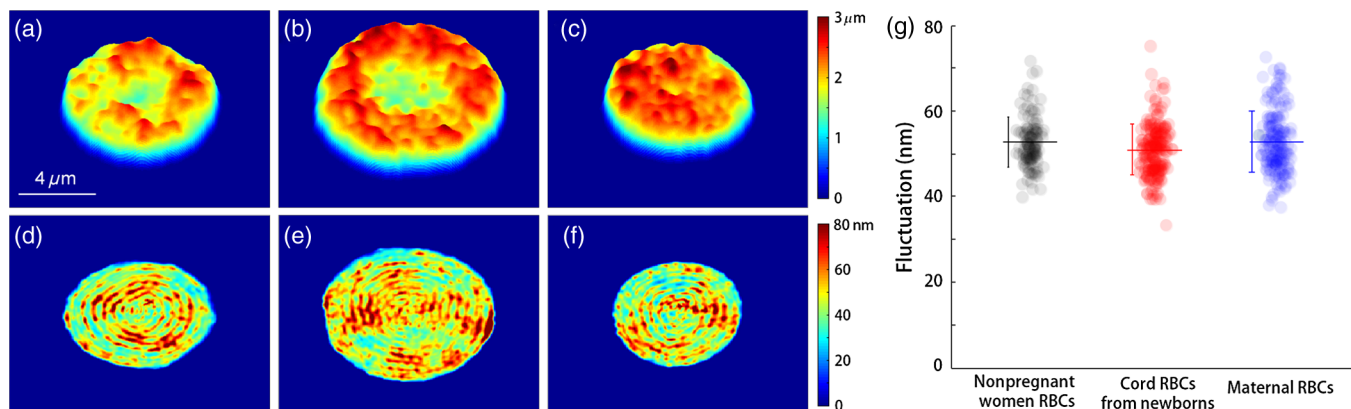
Fig. 4 (a) to (c) Representative two-dimensional topographic images of RBCs from nonpregnant women, and the cord blood of a newborn infant and a mother, respectively. (d) to (f) Their corresponding dynamic membrane fluctuations. The color bar scales are in μm (top row) and nm (bottom), respectively. (g) The averaged membrane fluctuations of individual RBCs in each group: nonpregnant women (black circles), cord blood of full-term newborn infants (red circles), and their mothers (blue circles). The horizontal solid line is the mean value; the vertical lines are the STD error bars.

The instantaneous displacement maps of the dynamic membrane fluctuations are shown in Figs. 4(d)–4(f).

To quantify the deformability of individual RBCs, the membrane fluctuations were calculated as the spatially averaged root mean squared (RMS) height displacement [Fig. 4(g)]. The representative membrane fluctuations of an RBC from the blood of a nonpregnant adult, cord blood, and maternal blood are presented in Figs. 4(d)–4(f), respectively. The RMS height displacements of the cord RBC are homogenous over the cell area, and compatible with those of the nonpregnant adult RBC and maternal RBC. The mean values of the membrane fluctuations were 52.7 ± 5.8, 50.9 ± 5.9, and 52.7 ± 7.1 nm for the RBCs from the nonpregnant women, the cord RBCS, and maternal RBCs, respectively. There were no statistical differences in the membrane fluctuations among the three groups of RBCs, indicating that cellular deformability of the cord RBCs and of the other RBCs were not significantly altered, despite considerable differences in cell volume and surface area.

4 Discussion

We presented the measurements for the morphological, biochemical, and mechanical characteristics of individual cord RBCs and maternal RBCs. Quantitative, noninvasive measurements of the RBCs using cDOT, 3-D RI maps, and dynamic membrane fluctuations were made. From these, the following important red cell parameters were retrieved systematically: cell volume, surface area, sphericity, Hb content, Hb concentration, and membrane fluctuation. The measured values for cell volume, Hb content, and Hb concentration were consistent with the independent CBC measurements, and also with previous reports.[7] To the best of our knowledge, this is the first report on experimental measurements for surface area, sphericity, and membrane fluctuations of cord and matching maternal RBCs.

We should note that the cDOT measurements provide more detailed information about individual RBCs from cord blood compared to existing CBC blood tests. For example, cDOT provides visualization of the structural details of RBCs (e.g., 3-D shape, surface area, and sphericity), whereas the CBC measurement only provides cell sizes from impedance measurements. cDOT also provides chemical information about individual RBCs, whereas the CBC test measures ensemble averaged information. Furthermore, deformability measurements are not available with CBC blood tests.

Our results from cDOT clearly show that the cord RBCs of full-term newborn infants have a significantly different morphology from the RBCs of nonpregnant women. The volume and surface area of the cord RBCs were 14 and 30% larger, respectively, than those of the RBCs from the nonpregnant women. The sphericity of the cord RBCs was 11% less than that of the RBCs from the nonpregnant women, indicating that the cord RBCs have more flattened shapes. The Hb content in the cord RBCs of newborns was significantly greater: the Hb content of the cord RBCs was 22 and 18% greater than that of the nonpregnant adult and maternal RBCs, respectively. In addition, the Hb concentration in the cord RBCs was higher than that of the nonpregnant women RBCs or maternal RBCs, but they were within the physiological range of adults. Interestingly, the amplitudes of the dynamic membrane fluctuations in the cord RBCs were comparable to those in the nonpregnant women RBCs and maternal RBCs, suggesting that the deformability of the cord RBCs is similar to that of healthy RBCs in adults.

It is speculated that these differences in the cord RBCs might evolve to meet the demand for high oxygen consumption by the fetus. An enlarged cell volume with a higher Hb concentration in the cord RBCs could carry oxygen to fetal tissues more efficiently. Because the high oxygen-binding affinity of HbF in the cord RBCs facilitates the transport of oxygen between two different circulatory systems through the umbilical cord, the unique morphological and biochemical properties of the cord blood enhance oxygen transport from the placenta to the fetus.

The question then arises whether this remodeling of the cord RBCs is beneficial or detrimental to fetal blood circulation. Although this question is not directly addressed by the current study, our measurements of the membrane fluctuations suggest that the cord RBCs may not be significantly different from other healthy RBCs in their ability to pass through small capillaries and restore themselves to their original shapes. This is based on their remarkably soft and elastic properties. Despite the enlarged cell volumes in the cord RBCs, their decreased sphericity indicates more discocytic shapes than that exhibited by healthy RBCs in adults, suggesting that the cord RBCs may still have good ability to pass through narrow passages. RBCs with low sphericity, or discocytes, have advantages to pass through narrow passages, compared to stomatocytes or echinocytes with high sphericity.[50,51] This ability has been attributed to the fact that RBCs with low sphericity have higher surface-to-volume ratios, which are beneficial for undergoing large deformation and restoration that occur when passing through small capillaries during microcirculation.[52–54]

The measured dynamic membrane fluctuations of the cord RBCs, the maternal RBCs, and the nonpregnant adult RBCs are not significantly different from one another. This result is consistent with a previous study using osmotic frangibility, which reported indistinguishable cellular deformability between full-term newborn infants and adults RBCs.[9] However, considering that other macrocytic RBCs produced due to various clinical situations, including anemia and chronic alcoholism,[55,56] exhibited more deformable RBCs, it is intriguing that the cord RBCs with enlarged cell volumes exhibit dynamic membrane fluctuations comparable to healthy RBCs. In addition, the maternal RBCs exhibit a loss of the characteristic dimple shapes and become sphere-like. However, the loss of dimple shapes found in ATP-depleted RBCs accompanied decreases in membrane fluctuations, which was not the case in the measured maternal RBCs. Taken together, our results imply complex remodeling in the membrane cortex structures in the cord RBCs and maternal RBCs.

We presented the optical measurements for the morphological, biochemical, and mechanical properties of individual cord RBCs and performed a comprehensive comparative analysis of maternal RBCs and nonpregnant healthy RBCs. The present method will open possibilities for diagnosis of diseases in newborn infants and their mothers, as well as for the study of the pathophysiology of cord RBCs and their implications in fetal circulation. From a technical point of view, the use of a quantitative phase imaging unit can convert an existing microscope into quantitative phase microscope[57–59] and will further expand the applicability of the present technique.

References

1. N. A. Murray and I. A. Roberts, "Haemolytic disease of the newborn," *Arch. Dis. Child Fetal Neonatal Ed.* **92**(2), F83–88 (2007).

2. Y. Matoth, R. Zaizov, and I. Varsano, "Postnatal changes in some red cell parameters," *Acta Paediatr.* **60**(3), 317 (1971).

3. U. M. Saarinen and M. A. Siimes, "Developmental-changes in red blood-cell counts and indexes of infants after exclusion of iron-deficiency by laboratory criteria and continuous iron supplementation," *J. Pediatr.* **92**(3), 412–416 (1978).

4. F. A. Oski, "The unique fetal red cell and its function. E. Mead Johnson Award address," *Pediatrics* **51**(3), 494–500 (1973).

5. R. E. Benesch, N. Maeda, and R. Benesch, "2, 3-Diphosphoglycerate and the relative affinity of adult and fetal hemoglobin for oxygen and carbon monoxide," *BBA* **257**(1), 178–182 (1972).

6. H. S. Maurer, R. E. Behrman, and G. R. Honig, "Dependence of the oxygen affinity of blood on the presence of foetal or adult haemoglobin," *Nature* **227**(5256), 388–390 (1970).

7. K. Kaushansky and W. J. Williams, *Williams Hematology*, McGraw-Hill Medical, New York (2010).

8. H. A. Pearson, "Life-span of the fetal red blood cell," *J. Pediatr.* **70**(2), 166–171 (1967).

9. M. L. Bautista et al., "Cord blood red cell osmotic fragility: a comparison between preterm and full-term newborn infants," *Early Hum. Dev.* **72**(1), 37–46 (2003).

10. M. Zhurova, J. Akabutu, and J. Acker, "Quality of red blood cells isolated from umbilical cord blood stored at room temperature," *J. Blood Transfus.* **2012**, 102809 (2012).

11. K. Eguchi, T. Sawai, and Y. Mizutani, "Erythrocyte deformability of nonpregnant, pregnant, and fetal blood," *J. Perinat. Med.* **23**(4), 301–306 (1995).

12. K. Eguchi et al., "Comparative study of erythrocyte deformability in maternal and cord blood," *Am. J. Perinatol.* **12**(1), 39–43 (1995).

13. G. P. Gross and W. E. Hathaway, "Fetal erythrocyte deformability," *Pediatr. Res.* **6**(7), 593–599 (1972).

14. G. Popescu, *Quantitative Phase Imaging of Cells and Tissues*, McGraw-Hill Professional, New York (2011).

15. K. Lee et al., "Quantitative phase imaging techniques for the study of cell pathophysiology: from principles to applications," *Sensors* **13**(4), 4170–4191 (2013).

16. P. Marquet, C. D. Depeursinge, and P. Magistretti, "Exploring neural cell dynamics with digital holographic microscopy," *Annu. Rev. Biomed. Eng.* **15**, 407–431 (2013).

17. M. K. Kim, "Principles and techniques of digital holographic microscopy," *SPIE Rev.* **1**(1), 018005 (2010).

18. Y. Kim, K. Kim, and Y. Park, "Measurement techniques for red blood cell deformability: recent advances," in *Blood Cell—An Overview of Studies in Hematology*, T. E. Moschandreou, Ed., pp. 167–194, INTECH, Rijeka, Croatia(2012).

19. G. Popescu et al., "Imaging red blood cell dynamics by quantitative phase microscopy," *Blood Cells, Mol., Dis.* **41**(1), 10–16 (2008).

20. S. Cho et al., "Optical imaging techniques for the study of malaria," *Trends Biotechnol.* **30**(2), 71–79 (2012).

21. H. Byun et al., "Optical measurement of biomechanical properties of individual erythrocytes from a sickle cell patient," *Acta Biomater.* **8**(11), 4130–4138 (2012).

22. Y. Park et al., "Spectroscopic phase microscopy for quantifying hemoglobin concentrations in intact red blood cells," *Opt. Lett.* **34**(23), 3668–3670 (2009).

23. Y. Park et al., "Metabolic remodeling of the human red blood cell membrane," *Proc. Natl. Acad. Sci.* **107**(4), 1289 (2010).

24. Y. Park et al., "Measurement of red blood cell mechanics during morphological changes," *Proc. Natl. Acad. Sci.* **107**(15), 6731 (2010).

25. Y. Park et al., "Refractive index maps and membrane dynamics of human red blood cells parasitized by *Plasmodium falciparum*," *Proc. Natl. Acad. Sci.* **105**(37), 13730 (2008).

26. B. Rappaz et al., "Spatial analysis of erythrocyte membrane fluctuations by digital holographic microscopy," *Blood Cells, Mol., Dis.* **42**(3), 228–232 (2009).

27. N. T. Shaked et al., "Quantitative microscopy and nanoscopy of sickle red blood cells performed by wide field digital interferometry," *J. Biomed. Opt.* **16**(3), 030506 (2011).

28. Y. Park et al., "Measurement of the nonlinear elasticity of red blood cell membranes," *Phys. Rev. E* **83**(5), 051925 (2011).

29. R. Chandramohanadas et al., "Biophysics of malarial parasite exit from infected erythrocytes," *PLoS One* **6**(6), e20869 (2011).

30. M. Diez-Silva et al., "Pf155/RESA protein influences the dynamic micro-circulatory behavior of ring-stage *Plasmodium falciparum* infected red blood cells," *Sci. Rep.* **2**, 614 (2012).

31. T. Betz et al., "ATP-dependent mechanics of red blood cells," *Proc. Natl. Acad. Sci. USA* **106**(36), 15320–15325 (2009).

32. Y. Kim et al., "Common-path diffraction optical tomography for investigation of three-dimensional structures and dynamics of biological cells," *Opt. Express* **22**(9), 10398–10407 (2014).

33. S. Shin et al., "Common-path diffraction optical tomography with a low-coherence illumination for reducing speckle noise," *Proc. SPIE* **9336**, 933629 (2015).

34. Y. Kim et al., "Profiling individual human red blood cells using common-path diffraction optical tomography," *Sci. Rep.* **4**, 6659 (2014).

35. J. Yoon et al., "Label-free characterization of white blood cells by measuring 3D refractive index maps," arXiv preprint arXiv:1505.02609 (2015).

36. H. Park et al., "Characterizations of individual mouse red blood cells parasitized by Babesia microti using 3-D holographic microscopy," *Sci. Rep.* **5**, 10827 (2015).

37. S. Lee et al., "High-resolution 3-D refractive index tomography and 2-D synthetic aperture imaging of live phytoplankton," *J. Opt. Soc. Korea* **18**(6), 691–697 (2014).

38. S. Lee et al., "Quantitative morphological and biochemical studies on human downy hairs using 3-D quantitative phase imaging," *J. Biomed. Opt.* **20**(11), 111207 (2015).

39. K. Kim et al., "High-resolution three-dimensional imaging of red blood cells parasitized by *Plasmodium falciparum* and in situ hemozoin crystals using optical diffraction tomography," *J. Biomed. Opt.* **19**(1), 011005 (2014).

40. J. Lim et al., "Comparative study of iterative reconstruction algorithms for missing cone problems in optical diffraction tomography," *Opt. Express* **23**(13), 16933–16948 (2015).

41. G. Tomaiuolo et al., "Comparison of two flow-based imaging methods to measure individual red blood cell area and volume," *Cytometry A* **81**(12), 1040–1047 (2012).

42. H. V. Pham et al., "Real time blood testing using quantitative phase imaging," *PLoS One* **8**(2), e55676 (2013).

43. H. G. Davies and M. H. Wilkins, "Interference microscopy and mass determination," *Nature* **169**(4300), 541 (1952).

44. G. Popescu et al., "Optical imaging of cell mass and growth dynamics," *Am. J. Physiol. Cell Physiol.* **295**(2), C538–544 (2008).

45. P. Ruef and O. Linderkamp, "Deformability and geometry of neonatal erythrocytes with irregular shapes," *Pediatr. Res.* **45**(1), 114–119 (1999).

46. F. Brochard and J. F. Lennon, "Frequency spectrum of flicker phenomenon in erythrocytes," *J. Phys. Paris* **36**(11), 1035–1047 (1975).

47. P. G. de Gennes, "Soft matter," *Science* **256**(5056), 495–497 (1992).

48. J. Evans et al., "Fluctuations of the red blood cell membrane: relation to mechanical properties and lack of ATP dependence," *Biophys. J.* **94**(10), 4134–4144 (2008).

49. S. Tuvia et al., "Mechanical fluctuations of the membrane-skeleton are dependent on F-actin ATPase in human erythrocytes," *J. Cell Biol.* **141**(7), 1551–1561 (1998).

50. M. Diez-Silva et al., "Shape and biomechanical characteristics of human red blood cells in health and disease," *MRS Bull.* **35**(5), 382–388 (2010).

51. H. W. G. Lim, M. Wortis, and R. Mukhopadhyay, "Stomatocyte-discocyte-echinocyte sequence of the human red blood cell: evidence for the bilayer-couple hypothesis from membrane mechanics," *Proc. Natl. Acad. Sci. USA* **99**(26), 16766–16769 (2002).

52. P. B. Canham, "The minimum energy of bending as a possible explanation of the biconcave shape of the human red blood cell," *J. Theor. Biol.* **26**(1), 61–81 (1970).

53. W. Helfrich, "Elastic properties of lipid bilayers: theory and possible experiments," *Z. Naturforsch. C* **28**(11), 693–703 (1973).
54. J. Li et al., "Spectrin-level modeling of the cytoskeleton and optical tweezers stretching of the erythrocyte," *Biophys. J.* **88**(5), 3707–3719 (2005).
55. M. R. Clemens et al., "Plasma and red cell lipids in alcoholics with macrocytosis," *Clin. Chim. Acta* **156**(3), 321–328 (1986).
56. K. W. Unger and D. Johnson Jr., "Red blood cell mean corpuscular volume: a potential indicator of alcohol usage in a working population," *Am. J. Med. Sci.* **267**(5), 281–289 (1974).
57. K. Kim et al., "Diffraction optical tomography using a quantitative phase imaging unit," *Opt. Lett.* **39**(24), 6935–6938 (2014).
58. K. Lee and Y. Park, "Quantitative phase imaging unit," *Opt. Lett.* **39**(12), 3630–3633 (2014).
59. S. Shin et al., "Active illumination using a digital micromirror device for quantitative phase imaging," arXiv preprint arXiv:1506.06237 (2015).

HyunJoo Park received her PhD in physics from KAIST. Since 2013, she has worked as a postdoctoral fellow at KAIST.

Taegyu Ahn is a clinical professor in the Department of Obstetrics & Gynecology, Kangwon National University. He completed his residency training and received his master's degree in obstetrics and gynecology from Kangwon National University. He is currently a PhD candidate.

Kyoohyun Kim received his BS degree in physics from KAIST. He is currently a PhD student at KAIST in the Department of Physics.

SangYun Lee received his BS degree in physics from KAIST. He is currently a PhD student at KAIST in the Department of Physics.

Song-yi Kook received his BS degree in life sciences from the University of Gachon Medical School and his MD degree from the School of Medicine, Kangwon National University, Kangwon, Korea.

Dongheon Lee is a professor in the medical school of Kangwon National University. He received his MD degree from Seoul National University and his PhD in gynecologic oncology from Ulsan University. He was a visiting scholar in the Department of Reproductive Endocrinology at medical school of Yale University during 2006 to 2007. He is a gynecologic oncologist, and his research interest is focusing on the apoptotic processes of rapidly growing cells.

In Bum Suh is an associate professor of laboratory medicine, College of Medicine, Kangwon National University, director of the Department of Laboratory Medicine, Kangwon National University Hospital, and the president of the Korea Clinical Medicine Center. He received his MD and PhD degrees from the College of Medicine, Korea University, in 1993 and 2002, respectively.

Sunghun Na is an obstetrician and a professor of the medical school of Kangwon National University, Korea. He received his MD degree from Chungnam National University, Korea, and PhD in maternal fetal medicine of obstetrics and gynecology from Ulsan University, Korea. He is scheduled to work as a visiting professor in the Department of Immunology at the medical school of Brown University from 2015 to 2016. His research interest is maternal fetal pathophysiology.

YongKeun Park is an associate professor in the Department of Physics, KAIST. He received his PhD in medical physics and medical engineering from Harvard-MIT Health Science and Technology in 2010 and joined KAIST. To learn more about his research projects, visit his website: http://bmol.kaist.ac.kr.